



SPE 106115

Numerical Simulation of Hydraulic Fracturing in the Viscosity-Dominated Regime

A.P. Bungler, SPE, CSIRO Petroleum; E. Detournay, SPE, U. of Minnesota; D.I. Garagash, Clarkson U.; and A.P. Peirce, U. of British Columbia

Copyright 2007, Society of Petroleum Engineers

This paper was prepared for presentation at the 2007 SPE Hydraulic Fracturing Technology Conference held in College Station, Texas, U.S.A., 29–31 January 2007.

This paper was selected for presentation by an SPE Program Committee following review of information contained in an abstract submitted by the author(s). Contents of the paper, as presented, have not been reviewed by the Society of Petroleum Engineers and are subject to correction by the author(s). The material, as presented, does not necessarily reflect any position of the Society of Petroleum Engineers, its officers, or members. Papers presented at SPE meetings are subject to publication review by Editorial Committees of the Society of Petroleum Engineers. Electronic reproduction, distribution, or storage of any part of this paper for commercial purposes without the written consent of the Society of Petroleum Engineers is prohibited. Permission to reproduce in print is restricted to an abstract of not more than 300 words; illustrations may not be copied. The abstract must contain conspicuous acknowledgment of where and by whom the paper was presented. Write Librarian, SPE, P.O. Box 833836, Richardson, TX 75083-3836, U.S.A., fax 01-972-952-9435.

Abstract

Most hydraulic fracturing treatments are in the viscosity-dominated regime. Hence, fracture growth does not depend on the rock toughness and it can be shown that the fracture aperture w near the fracture front, when viewed at the scale of the whole fracture, is not characterized by the classical square root behavior predicted by linear elastic fracture mechanics $w \sim s^{1/2}$, where s is the distance from the tip. Instead, the asymptotic tip aperture that reflects the predominance of viscous dissipation is of the form $w \sim s^{2/3}$, under conditions of large efficiency and small fluid lag. After demonstrating the intimate connection between the tip aperture and the fracture propagation regime, we report the results of hydraulic fracturing laboratory experiments in PMMA and glass blocks that employ a novel optical technique to measure the fracture opening. These experiments provide incontrovertible evidence that the power law index, characterizing the fracture aperture near the tip, depends on the propagation regime in accordance with theoretical findings. Finally, we demonstrate that a coarsely-meshed planar hydraulic fracture simulator can produce accurate results relative to benchmark solutions provided that the appropriate tip behavior is embedded in the algorithm. Through theoretical, experimental, and computational considerations, these results make it clear that advances in the accuracy and efficiency of fracture simulators critically depend on a sophisticated treatment of the near-tip aperture that goes beyond basic linear elastic fracture considerations.

Introduction

Fluid-driven fractures represent a particular class of tensile fractures that propagate in solid media, typically under preexisting compressive stresses, as a result of internal pressurization by an injected viscous fluid. Hydraulic fractures are most commonly engineered for the stimulation of hydrocarbon-bearing rock strata to increase the production of oil and gas

wells [1-3], but there are other industrial applications such as remediation projects in contaminated soils [4-6], waste disposal [7,8], excavation of hard rocks [9], preconditioning and cave inducement in mining [10,11]. Furthermore, hydraulic fractures manifest at the geological scale as kilometer-long vertical dikes bringing magma from deep underground chambers to the earth's surface [12-14], or as subhorizontal fractures known as sills that divert magma from dikes [15-17].

Since the pioneering work by Kristianovitch and Zheltov [18], there have been numerous contributions on the modeling of fluid-driven fractures that have been mainly motivated by the application of hydraulic fracturing to the stimulation of oil and gas wells. The early efforts naturally focused on analytical solutions for fractures having simple geometries, either along straight lines in plane strain or penny-shaped in situations of radial symmetry [18-25]. However, all these solutions were approximate as they contain strong assumptions about either the opening or the pressure field. In recent years, the limitations of these solutions have shifted the focus of research towards the development of numerical algorithms, to model the three-dimensional propagation of hydraulic fractures in layered strata characterized by different mechanical properties and/or in-situ stresses [26-33].

Most of the hydraulic fracture simulators that are freed of *a priori* constraints on the fracture shape and of the approximations associated with models commonly referred to as “Pseudo-3D,” are based on linear elastic fracture mechanics (LEFM); this is reflected by the imposition of a square root asymptotic behavior on the fracture aperture, $w \sim s^{1/2}$ (where s is the distance from the crack front) in the tip region. As it is well known, the square root asymptote is intimately linked to the energy dissipated in the creation of new fracture surfaces in the rock [34]. However, it was progressively realized in the late 1980's and early 1990's [35-37] that another tip asymptote of the form $w \sim s^{2/3}$ (for a Newtonian fluid and in the absence of leak-off) arises under conditions where the energy in the tip region of a propagating fracture is essentially dissipated in viscous flow. These results then motivated a systematic reexamination of the classical KGD and penny-shaped fractures [38-49] as well as the construction of comprehensive tip asymptotics that incorporate toughness, leak-off, viscous flow and the existence of a lag between the fluid front and the crack edge [50-54].

The first practical outcome of these rigorous studies was the

recognition that several time scales control the evolution of a hydraulic fracture. One of the time scales is associated with the transition between a regime of propagation where the energy input of mechanical work at the wellbore is essentially dissipated in viscous flow of the fracturing fluid and another regime where most of the energy is used to fracture the rock. A second time scale characterizes the evolution from situations where the injected fluid is essentially stored in the fracture (efficiency close to 100%) to situations where most of the fluid has leaked into the rock (vanishing efficiency). A third time scale is linked to the progressive disappearance of the lag between the fracturing fluid front and the fracture tip, and depends, among other parameters, on the magnitude of the in-situ stress and pore pressure. However, a parametric analysis indicates that, for most hydraulic fracturing treatments, only the time scale associated with the change of efficiency is relevant. Indeed, the time scale associated with the transition from the viscosity- to the toughness-dominated regime is typically very large compared to the treatment time, while the time scale associated with the vanishing of the lag is typically very small compared to the treatment time. In short, most hydraulic fractures for reservoir stimulations propagate in the viscosity-dominated regime under conditions in which the fluid front coincides with the fracture front.

The second outcome of these research activities was the realization that the combination of the square root tip asymptote and the relatively small number of discretization cells (of order $O(100 \sim 1000)$) typically used in numerical computations artificially forces the fracture to propagate in the toughness-dominated regime. In other words, simulation of a hydraulic fracture in the viscosity-dominated regime requires the imposition of a different tip asymptote, whose strength depends on the tip velocity.

This paper describes a preliminary effort to construct a hydraulic fracture simulator that incorporates the viscosity asymptote, under the restricted conditions of zero leak-off. After a description of the equations governing this problem both at the global scale of the fracture and at the tip scale, we show incontrovertible experimental evidence that the fracture aperture near the tip behaves according to $w \sim s^{2/3}$ in the viscosity-dominated regime and according to $w \sim s^{1/2}$ in the toughness-dominated regime. Finally, we show that a coarsely-meshed planar hydraulic fracture simulator produces accurate results relative to benchmark solutions provided that the appropriate tip behavior is embedded in the algorithm.

Mathematical Model

Governing Equations

The equations governing the propagation of a hydraulic fracture in a reservoir have to account for the dominant physical mechanisms taking place during the treatment, namely deformation of the rock, creation of new fracture surfaces, flow of the fracturing fluid in the crack, formation of a cake, and leak-off of the fracturing fluid into the reservoir. Besides the standard assumptions regarding the applicability of linear elastic fracture mechanics (LEFM) and lubrication theory, we make a series of simplifications that can readily be justified for the

purpose of this contribution: (i) leak-off is neglected, (ii) the rock is homogeneous (toughness K_{Ic} , Young's modulus E , and Poisson ratio ν thus have uniform values), (iii) the fracturing fluid is incompressible and Newtonian (viscosity μ), (iv) the fracture is always in limit equilibrium, (v) gravity is neglected in the lubrication equation, and (vi) the fluid front coincides with the crack front, because the lag between the two fronts is negligible under typical conditions of reservoir stimulation [49,50]. With these assumptions, the fracture aperture $w(x, y, t)$, the fluid pressure $p_f(x, y, t)$, and the position of the front $C(t)$ are governed by the following set of equations (Figure 1):

- *Elasticity equation*

$$p_f - \sigma_o = -\frac{E'}{8\pi} \int_{S(t)} \frac{w(x', y', t) dS(x', y')}{[(x' - x)^2 + (y' - y)^2]^{3/2}} \quad (1)$$

where $S(t)$ denotes the fracture footprint (enclosed by the crack front $C(t)$ and having a characteristic dimension $L(t)$), and $\sigma_o(x, y)$ is the far-field compressive stress perpendicular to the fracture plane (and a known function of position);

- *Reynolds equation*

$$\frac{\partial w}{\partial t} = \frac{1}{\mu} \nabla \cdot (w^3 \nabla p_f) + Q(t) \delta(x, y) \quad (2)$$

where $\delta(x, y)$ denotes the Dirac delta function, with the origin of the system of coordinates (x, y) taken to coincide with the injection point, and $Q(t)$ is the volumetric injection rate (a given function of time);

- *Boundary conditions at the moving front $C(t)$*

$$\lim_{s \rightarrow 0} \frac{w}{s^{1/2}} = \frac{K'}{E'}, \quad \lim_{s \rightarrow 0} w^3 \frac{\partial p_f}{\partial s} = 0 \quad (3)$$

where s denotes the distance from the crack front $C(t)$ (with the s -axis directed inwards). The first condition (3) is a classical result of LEFM, while the second simply expresses a no-flux boundary condition at the fracture tip.

The material parameters E' , K' , and μ'

$$E' = \frac{E}{1 - \nu^2}, \quad K' = 4 \left(\frac{2}{\pi} \right)^{1/2} K_{Ic}, \quad \mu' = 12\mu \quad (4)$$

have been introduced to keep equations uncluttered by numerical factors; for convenience, they are referred to as the elastic modulus, the toughness, and the viscosity.

The system of equations (1)-(3) is closed and can, in principle, be solved to determine the evolution of a hydraulic fracture, given appropriate initial conditions. However, the accurate numerical solution of this system represents a formidable problem, despite the apparent simple form of the equations. Indeed, three challenging issues arise from the structure of the mathematical model: (i) the *non-locality* of the elastic re-

sponse of the fracture (meaning that the opening w at one point of the fracture depends on the fluid pressure p_f at another point), (ii) the *non-linearity* originating from the dependence of the fracture conductivity on the cube of the crack opening, and (iii) the *moving boundary* associated with the propagating crack front. These challenges have been well-known since the late 1970's when numerical methods specifically designed to solve this class of problems were first developed [26], and still remain to this date as evidenced by the ongoing drive to improve the efficiency of the computational algorithms [55].

Only recently, however, has it been appreciated that the non-local and non-linear nature of the governing equations, combined with the fracture propagation criterion, conspire to yield a multiscale structure of the solution near the fracture tip [50,51,42,53]. In particular, there are conditions – actually prevalent in hydraulic fracturing treatments – when the classical square root asymptote of linear elastic fracture mechanics exists at such a small scale that it cannot be resolved at the discretization length used to conduct the computations. Under these conditions, which correspond to the viscosity-dominated regime of fracture propagation, significant errors in the prediction of the fracture dimension and width result from imposing an asymptotic behavior that is not relevant at the grid size used to carry out the computations. That the behavior of the solution in the tip region has such an overwhelming influence on the global response of the hydraulic fracture is to be expected from the nature of the problem where only the volume of the fracture is constrained (which is not even the case when leak-off is taken into account).

It will be made clear in the following, that numerical simulators for hydraulic fractures must account the multiscale nature of the solution in the tip region, to ensure accurate predictions.

Scaling

Before summarizing the behavior of the solution in the tip region, it is useful to scale the governing equations. Thus, we introduce a length scale L_* , a time scale T_* , a characteristic fracture aperture W_* , and a characteristic (net) pressure P_* (all yet to be defined). The physical quantities of the problem are thus formally expressed as

$$x = L_*\chi, \quad y = L_*\zeta, \quad t = T_*\tau, \quad w = W_*\Omega, \quad p_f = P_*\Pi_f \quad (5)$$

By introducing the above relations in the governing equations, it can readily be shown that four dimensionless groups emerge

$$G_e = \frac{L_*P_*}{E'W_*}, \quad G_m = \frac{\mu' L_*^2}{P_*T_*W_*^2}, \quad G_k = \frac{K' L_*^{1/2}}{E'W_*}, \quad G_v = \frac{Q_o T_*}{L_*W_*} \quad (6)$$

where Q_o is the characteristic injection rate, $Q(t) = Q_o\psi(\tau)$, with $\psi(\tau)$ representing a dimensionless injection schedule. Then, setting $G_e = G_m = G_k = G_v = 1$ yields four conditions to identify L_* , T_* , P_* , and W_*

$$L_* = \frac{Q_o\mu'E'^3}{K'^4}, \quad T_* = \left(\frac{Q_o^3\mu'^5E'^{13}}{K'^{18}} \right)^{1/2}, \quad (7)$$

$$W_* = \left(\frac{Q_o\mu'E'}{K'^2} \right)^{1/2}, \quad P_* = \left(\frac{K'^6}{Q_o\mu'E'^3} \right)^{1/2}$$

On the one hand, the condition $G_e = 1$ simply means that the average aperture scaled by the fracture dimension is of the same order as the average net pressure scaled by the elastic modulus, in accordance to elementary elasticity considerations. On the other hand, the conditions $G_m = G_k = 1$ (with G_m and G_k having the meaning of a dimensionless viscosity and toughness, respectively) imply that T_* reflects the time of transition between a viscosity and a toughness-dominated regime, since equal weight is placed on viscosity and toughness. Actually, calculation for a penny-shaped fracture propagating under a constant injection rate Q_o indicates that T_* effectively marks the end of the viscosity-dominated regime. Finally, the condition $G_v = 1$ guarantees that L_* is the characteristic dimension of the fracture at $t = T_*$.

This scaling ensures that for an ideal case, characterized by uniform properties and stress (which obviously leads to the formation of a penny-shaped fracture) as well as a constant injection rate, all the problem parameters (Q_o , K' , E' , and μ') are embodied in the scaling factors, noting that σ_o serves only as a reference for the fluid pressure, in the absence of a lag. Finally, the governing equations transform in the numerical scaling as follows:

$$\Pi_f - \Sigma_o = -\frac{1}{8\pi} \int_{S(\tau)} \frac{\Omega(\chi', \zeta', \tau) dS(\chi', \zeta')}{\left[(\chi' - \chi)^2 + (\zeta' - \zeta)^2 \right]^{3/2}} \quad (8)$$

$$\frac{\partial \Omega}{\partial \tau} = \nabla \cdot (\Omega^3 \nabla \Pi_f) + \psi(\tau) \delta(\chi, \zeta) \quad (9)$$

$$\lim_{\xi \rightarrow 0} \frac{\Omega}{\xi^{1/2}} = 1, \quad \lim_{\xi \rightarrow 0} \Omega^3 \frac{\partial \Pi_f}{\partial \xi} = 0 \quad (10)$$

where Σ_o is the scaled far-field stress σ_o / P_* . Note that it is advantageous to introduce the net pressure $\Pi = \Pi_f - \Sigma_o$, if Σ_o is homogeneous. The characteristic dimension of the fracture (e.g., the fracture radius) is $\gamma(\tau) = L / L_*$.

Finally, we note that the tip velocity V , the critical quantity that legislates the asymptotic behavior of the solution, is equal to the average fluid velocity in the tip region in the absence of leak-off. By introducing the scaling factor V_*

$$V_* = \left(\frac{K'^{10}}{Q_o\mu'^3E'^7} \right)^{1/2} \quad (11)$$

the scaled tip velocity $v = V / V_*$ can be expressed as

$$v = \lim_{\xi \rightarrow 0} \frac{1}{\Omega^2} \frac{\partial \Pi_f}{\partial \xi} \quad (12)$$

where ξ is the scaled distance from the fracture front. As shown below, the asymptotic solutions for Ω and Π_f depend only on ξ and v .

Tip Region

Theoretical Analysis

It can be shown [56] that the equations governing the aperture Ω and the net pressure $\Pi = \Pi_f - \Sigma_o$ in the vicinity of the fracture edge degenerate into

$$w^2 \frac{dp}{ds} = \mu' V, \quad p = \frac{E'}{4\pi} \int_0^\infty \frac{dw}{dz} \frac{dz}{s-z}, \quad \lim_{s \rightarrow 0} \frac{w}{s^{1/2}} = \frac{K'}{E'} \quad (13)$$

where the propagation velocity V is given by the instantaneous local propagation velocity of the fracture front (Figure 2). Note that the spatial variation of the far-field stress can generally be ignored when viewed at the tip scale, unless the stress field is discontinuous (in which case, the tip solution outlined here is not appropriate). Equations (13) are in fact identical to the governing equations for the problem of a semi-infinite fluid-driven fracture steadily propagating at constant velocity and characterized by zero lag [50,42]. In other words, the tip asymptotic solution is given at any time by the solution of the stationary semi-infinite crack problem with a constant tip velocity corresponding to the current propagation speed of the finite fracture. The tip solution is thus autonomous.

The tip asymptotics can be rewritten more advantageously in terms of a normalized distance from the tip $\hat{\xi}$, opening $\hat{\Omega}$, and net-pressure $\hat{\Pi}$, respectively defined as,

$$s = \hat{L}_* \hat{\xi}, \quad w = \hat{W}_* \hat{\Omega}, \quad p = \hat{P}_* \hat{\Pi} \quad (14)$$

where the tip length scale \hat{L}_* , the characteristic tip opening \hat{W}_* , and the characteristic pressure \hat{P}_* are given by

$$\hat{L}_* = \frac{K'^6}{E'^4 \mu'^2 V^2}, \quad \hat{W}_* = \frac{K'^4}{E'^3 \mu' V}, \quad \hat{P}_* = \frac{E'^2 \mu' V}{K'^2} \quad (15)$$

Through the tip scaling, the dependence of the asymptotic solution upon the material parameters μ' , E' , K' , as well as on the tip velocity V is entirely captured in the scaling factors \hat{L}_* , \hat{W}_* , and \hat{P}_* . In other words, the tip asymptotic solution has a universal form $\hat{\Omega}(\hat{\xi})$ and $\hat{\Pi}(\hat{\xi})$. Although the complete tip solution has to be computed numerically, its series expansion for small and large $\hat{\xi}$ is known explicitly [42]. The series expansion for $\hat{\Omega}(\hat{\xi})$ is given by

$$\hat{\xi} \rightarrow 0: \quad \hat{\Omega} = \hat{\xi}^{1/2} + 4\pi \hat{\xi} + \frac{128}{3} \hat{\xi}^{3/2} \ln \hat{\xi} + O(\hat{\xi}^{3/2}) \quad (16)$$

$$\hat{\xi} \rightarrow \infty: \quad \hat{\Omega} = \beta_0 \hat{\xi}^{2/3} + \beta_1 \hat{\xi}^h + o(\hat{\xi}^h) \quad (17)$$

where $\beta_0 = 2^{1/3} \cdot 3^{5/6}$, $\beta_1 \sim 0.0371887$, $h \sim 0.138673$. The complete semi-infinite tip solution is plotted in Figure 5, together with some experimental results (discussed below). It can be seen from this Figure that the LEFM behavior ($\hat{\xi}^{1/2}$) applies for $\hat{\xi} \leq \hat{\xi}_k \approx 10^{-5}$ and the viscosity dissipation asymptote ($\hat{\xi}^{2/3}$) for $\hat{\xi} \geq \hat{\xi}_m \approx 10^{-1}$.

The tip asymptote can readily be expressed in terms of $\Omega(\xi)$ from the relationship between the two scalings,

$$\hat{\Omega} = \frac{W_*}{\hat{W}_*} \Omega, \quad \hat{\xi} = \frac{L_*}{\hat{L}_*} \xi \quad (18)$$

which can be simplified as

$$\hat{\Omega} = v \Omega, \quad \hat{\xi} = v^2 \xi \quad (19)$$

Thus Ω behaves according to the viscosity asymptote, $\Omega \sim \beta_0 v^{1/3} \xi^{2/3}$ if $\xi \geq \hat{\xi}_m / v^2$, but according to the toughness asymptote $\Omega \sim \xi^{1/2}$ if $\xi \leq \hat{\xi}_k / v^2$.

Now consider a fracture for which the scaled extent is $\gamma = L / L_*$ so that size of the near-tip region is $\varepsilon \gamma$, where ε is a small number of order $O(10^{-2} \sim 10^{-1})$. In light of the above analysis, the relevance of either limiting asymptotic behavior, as far as the global solution is concerned, depends on the comparison of the length $\hat{\xi}_m / v^2$ or $\hat{\xi}_k / v^2$ with $\varepsilon \gamma$. Hence, the tip will be locally dominated by the viscosity asymptote if

$$\frac{1}{\gamma v^2} \leq \frac{\varepsilon}{\hat{\xi}_m} = O(0.1 \sim 1). \quad (20)$$

In contrast, the tip is expected to behave, at the global scale, according to the LEFM asymptote if

$$\frac{1}{\gamma v^2} \geq \frac{\varepsilon}{\hat{\xi}_k} = O(10^{-3} \sim 10^{-4}). \quad (21)$$

It is clear from this analysis that, for a given problem, the nature of the tip asymptote depends critically on the tip velocity. If the tip velocity is sufficiently large compared to a characteristic velocity (which is a function of the viscosity of the fracturing fluid, the toughness, and the elastic properties of the rock) then the tip solution is dominated at the fracture scale by the viscosity asymptote ($\Omega \sim \beta_0 v^{1/3} \xi^{2/3}$, with $\xi / \gamma = O(\varepsilon)$). However if the tip velocity is sufficiently small then the aper-

ture in the tip region is given by the LEFM asymptote ($\Omega \sim \xi^{1/2}$, with $\xi/\gamma = O(\varepsilon)$). This multiscale nature of the fracture tip is, in fact, related to a competition between two energy dissipation mechanisms, with domination of the LEFM asymptote corresponding to the predominance of energy dissipation due to creation of new surfaces in the rock while domination of the viscosity asymptote corresponds to the predominance of energy dissipation due to viscous flow. Furthermore, implementing this multiscale asymptote in numerical fracture simulators is essential in order to construct accurate solutions for finite fractures.

Experimental Validation

Laboratory experiments were performed in order to validate the hydraulic fracture tip solution. Circular hydraulic fractures were driven through Polymethyl Methacrylate (PMMA) or borosilicate glass specimens (200 x 200 x 150 mm), using fluids which were solutions of water, blue food dye, and either glycerine or glucose so that the dynamic viscosity μ was varied between 0.08 and 36 Pa·s. Note that the viscosity of these fluids depends strongly on the temperature, hence the measurement from a temperature probe (Figure 3) was used to compute the viscosity based on a calibrated relationship determined for each fluid using a Canon-Fenske viscometer [17].

The fractures were driven either through intact glass blocks ($E' = 75.3$ GPa, $K_{Ic} = 1.25$ MPa·m^{1/2}), or along a 0.01 mm thick, low toughness ($K_{Ic} = 0.38$ MPa·m^{1/2}), brittle epoxy interface in the case of the PMMA blocks ($E' = 3.93$ GPa), as indicated in Figure 3. Prior to and during the fracturing treatment, the specimens were loaded using water-filled flatjacks in a specially designed polyaxial reaction frame. The loading was applied so that σ_o varied from 5 to 16 MPa, which was sufficient in each case to prevent formation of a visible lag between the fluid and fracture fronts [50,57]. The lateral stress was then adjusted to be larger than the vertical stress so that horizontal fracture growth was promoted.

The polyaxial frame used here has the particular advantage that stresses can be applied perpendicular to the direction of eventual fracture opening while also permitting the growing fracture to be monitored continuously using a digital video camera. This capability relies both on a PMMA lower platen, which also serves as a light source, and on a transparent PMMA upper reaction plate (Figure 3). Using this light/camera apparatus with the transparent loading system and specimens, the fracture tip velocity was determined directly from the video images. Furthermore, the fracture opening w was determined from analysis of grayscale images of the growing fracture according to [58]

$$w(x, y) = k \log_{10} \frac{P_o(x, y)}{P(x, y)}, \quad (22)$$

where P_o and P_s are grayscale pixel values ($0 \leq P, P_o \leq 256$), with $P(x, y)$ corresponding to the value at

a location (x, y) within the fluid filled portion of the fracture and $P_o(x, y)$ giving the value at that same location prior to fracture growth. Here k is a factor determined by calibration with fluid-filled wedges for which the opening w was known. It has been demonstrated that this novel photometric technique is capable of measuring the full-field fracture opening within 10% accuracy provided that all lighting conditions are carefully controlled [57].

Figure 4 shows two contrasting examples of fracture tip opening profiles measured in this way. Each gives data from a single video frame recorded during fracture growth and analyzed according to (18). Both results give the average of the opening measured along 16 radial lines for these circular fractures. However, Figure 4a gives the results from a case where $1/\gamma v^2 = 1.8 \cdot 10^{11}$, as computed from the test parameters ($E' = 3.93$ GPa, $K_{Ic} = 0.38$ MPa·m^{1/2}, $\mu = 0.10$ Pa·s, $V = 3$ mm/s, $R = 20$ mm). In this case, as predicted by (21), the aforementioned tip structure does not develop and instead one only observes the LEFM ($w \propto s^{1/2}$) asymptote. In contrast, Figure 4b shows results for which $1/\gamma v^2 = 0.07$ ($E' = 3.93$ GPa, $K_{Ic} = 0.38$ MPa·m^{1/2}, $\mu = 28.9$ Pa·s, $V = 2$ mm/s, $R = 30$ mm), and one can see directly that the observable behavior of the fracture tip is predominantly described by the $w \propto s^{2/3}$ asymptote as predicted by (20).

Going a step further, a collection of results of the form shown in Figure 4 can be scaled according to (18) and presented together with the tip solution $\hat{\Omega}(\hat{\xi})$ [57]. Figure 5 shows results from 7 tests performed in epoxy-bonded PMMA blocks and 3 performed in glass specimens. The parameters for these tests were varied so that different asymptotic behaviors dominated the observable scale. Reported here are results from analysis of 3 to 8 video frames from each of the 10 tests, taking the outer 15% of the fracture as the tip region and ensuring that the fracture radius was no more than half of the distance to the nearest specimen boundary so that boundary effects were minimized. The experimental data exhibit some scatter, mainly due to the fact that the fracture opening becomes very small in the tip region which can be to the detriment of the signal to noise ratio for the measurements. Nonetheless, the close agreement between the experimental and analytical results for the fracture tip opening uphold the boundary layer solution that has been developed to describe the tip region of hydraulic fractures [57].

Numerical Algorithm

Method of Resolution

We now discuss the principles behind the multiscale fixed grid algorithm, implemented in the planar hydraulic fracture code MALIKA. The algorithm is built on a fixed computational grid consisting of a uniform mesh of rectangular constant displacement discontinuity (DD) elements for the elasticity computations [59], coupled with a five node finite difference stencil for the fluid flow calculations [33]. The computational

scheme further relies on dividing the fracture into two regions, the “Channel” representing the main part of the fracture, and the “Tip,” which is under the asymptotic umbrella, and on iterating at a each new time step between the solution in the Channel and that in the Tip. In fact, the Channel corresponds to the contiguous set of fully-filled elements, while the Tip is the set of partially filled elements at the periphery of the fracture. Tip elements exchange fluid only with Channel elements. Determining the solution in the Channel requires solving a system of non-linear equations obtained from discretizing the lubrication and elasticity equations, which are formulated in terms of the constant apertures of the DD elements as the primary unknowns. The solution in the Tip involves computing the location of the front in the partially filled elements, using the tip asymptotic volume and the current volume of fluid stored in the tip elements; the appropriate asymptotic behavior relies on the tip velocity, which is extrapolated from the fluid velocity at the Channel/Tip interface. Essentially, the current conditions at the tip enable one to determine how to map the analytic tip solution to a tip element by comparing the variable tip length scales with the tip element size. The local computation of the front position as well as that of the mean aperture of the tip elements is made possible by the one-dimensional nature of the tip asymptote. A critical issue of the proposed scheme is the accurate calculation of the local tip velocity, which directly influences the asymptotic behavior. The staggered computation scheme involves a two-way communication between the Channel and Tip calculations. Namely, a new estimate of the flux (magnitude and direction) is provided to the Tip at the end of a Channel calculation, while the Tip computation returns an updated aperture of the Tip elements, which affects the Channel solution via the non-local elasticity operator.

Discrete Equations

In order to simplify the discretization process we consider a uniform rectangular mesh with spacings $\Delta\chi$ and $\Delta\zeta$ in the two coordinate directions to encompass the region into which the fracture will move. The fracture surface S is therefore decomposed into rectangular elements S_{mn} such that $S = \cup S_{mn}$. The elasticity equation (1) is then discretized by assuming that the fracture opening $\Omega(\chi, \zeta, \tau)$ is piecewise constant over each rectangular element S_{mn} , i.e.

$$\Omega(\chi, \zeta, \tau) = \sum_{m,n} \Omega_{mn}(\tau) H_{mn}(\chi, \zeta)$$

in which $H_{mn}(\chi, \zeta) = \begin{cases} 1 & \text{for } (\chi, \zeta) \in S_{mn} \\ 0 & \text{for } (\chi, \zeta) \notin S_{mn} \end{cases}$ is the characteristic

function for the mn th element. Substituting this approximation into the integral equation (1) and evaluating the pressures at the collocation points comprising the element centres, yields a system of algebraic equations of the form:

$$\Pi_{kl}(\tau) = \sum_{m,n} C_{k-m,l-n} \Omega_{mn}(\tau) \quad (23)$$

where

$$C_{k-m,l-n} = -\frac{1}{8\pi} \left[\frac{\sqrt{(\chi_k - \chi)^2 + (\zeta_l - \zeta)^2}}{(\chi_k - \chi)(\zeta_l - \zeta)} \right]_{\chi=\chi_m+\Delta\chi, \zeta=\zeta_n+\Delta\zeta}^{\chi=\chi_m-\Delta\chi, \zeta=\zeta_n-\Delta\zeta}$$

In order to discretize the fluid flow equation (2) in a way that is compatible with (23), we use the pressures $\Pi_{kl}(\tau)$ and widths $\Omega_{kl}(\tau)$ at element centres along with central difference approximations of the partial derivatives to arrive at the following spatial discretization:

$$\frac{d}{d\tau} \Omega_{kl}(\tau) = \frac{1}{\Delta\chi} \left(\Omega_{k+\frac{1}{2}}^3 \frac{(\Pi_{k+1l} - \Pi_{kl})}{\Delta\chi} - \Omega_{k-\frac{1}{2}}^3 \frac{(\Pi_{kl} - \Pi_{k-1l})}{\Delta\chi} \right) + \frac{1}{\Delta\zeta} \left(\Omega_{kl+\frac{1}{2}}^3 \frac{(\Pi_{kl+1} - \Pi_{kl})}{\Delta\zeta} - \Omega_{kl-\frac{1}{2}}^3 \frac{(\Pi_{kl} - \Pi_{kl-1})}{\Delta\zeta} \right) \quad (24)$$

This system of ordinary differential equations applies in the channel region where the elements are completely filled with fluid. By eliminating the pressure $\Pi_{kl}(\tau)$ between (23) and (24) we obtain an extremely stiff system of nonlinear ordinary differential equations, which require an L -stable method such as the backward Euler scheme to march the solution forward in time. This requires the solution of a large system of nonlinear equations at each time step.

Tip and Channel

The nonlinear channel equations are solved by assuming a known trial solution for the tip elements. Once an equilibrium solution has been obtained for the channel elements, the widths of the channel elements are frozen and the tip solution is adjusted in the following way to match the overall volume balance between the two regions. On the boundary between the channel region and the tip region, the fluxes are evaluated to determine the volume of fluid in each tip element. These tip fluid volumes are then combined with the appropriate asymptotic solution to locate the fracture front. For example, if the applicable asymptotic power law is of the form $\Omega(\hat{\xi}) \sim c\hat{\xi}^\alpha$ then the tip volume $V(\ell)$ can be expressed in the form:

$$V(\ell) = c \int_0^\ell \hat{\xi}^\alpha \phi(\hat{\xi}) d\hat{\xi}$$

where $\hat{\xi}$ is the distance from the local fracture front, $\phi(\hat{\xi})$ is the local dimension of the current element in a direction parallel to the front, and ℓ is the distance between the front and the opposite vertex of the tip element. Average width values calculated from the tip fluid volumes are then allocated to the tip width values in order to set the current tip trial solution. With this new trial solution in the tip region we then proceed with the solution of the nonlinear channel equations. This process is repeated, until the front position and the channel and tip solutions all reach equilibrium.

Radial Fracture in the Viscosity Regime

Analytical Solution

The assumption of a uniform far-field stress σ_o , in addition to the other assumptions adopted earlier lead, necessarily to a radial fracture geometry. Furthermore we will restrict considerations to a constant injection rate Q_o from time $t=0$ (i.e., the pumping schedule function $\psi(\tau)=1$). The characteristic dimension L of the fracture at time t is naturally taken to be the fracture radius $R(t)$ and thus the scaled radius is $\gamma(\tau)=R/L_*$. The solution $F(\tau)$ is then of the form $\gamma(\tau)$, $\Omega(\rho,\tau)$, $\Pi(\rho,\tau)$ where ρ is the radial coordinate ($0 \leq \rho \leq \gamma(\tau)$) given by $\rho = \sqrt{\chi^2 + \zeta^2}$

It can be proven using scaling arguments [39,60] that the solution $F(\tau)$ degenerates into a self-similar solution both at small time

$$\gamma = \gamma_{mo} \tau^{4/9}, \Omega = \Omega_{mo} (\bar{\rho}) \tau^{4/9}, \Pi = \Pi_{mo} (\bar{\rho}) \tau^{-1/3}, \quad \tau \ll 1 \quad (25)$$

and at large time

$$\gamma = \gamma_{ko} \tau^{2/5}, \Omega = \Omega_{ko} (\bar{\rho}) \tau^{1/5}, \Pi = \Pi_{ko} \tau^{-1/5}, \quad \tau \gg 1 \quad (26)$$

where $\bar{\rho} = \rho/\gamma(\tau)$ noting that $0 \leq \bar{\rho} \leq 1$. More importantly, however, the small time similarity solution (25) corresponds to the viscosity dominated regime, and the large time solution (26) to the toughness dominated regime. Indeed, it can readily be shown, by reverting to the physical quantities using the scaling relationships (5), that the small time solution does not depend on the toughness, while the large time solution is independent of the viscosity. Furthermore, numerical simulations [39,48] indicate that the fracture propagates essentially in the viscosity dominated regime as long as $\tau \leq 1$ ($t \leq T_*$).

A first order approximation of the self-similar solution γ_{mo} , $\Omega_{mo}(\bar{\rho})$, $\Pi_{mo}(\bar{\rho})$ is given by [39]

$$\Omega_{mo}(\bar{\rho}) = \gamma_{mo} \left[\frac{\sqrt{70}}{3} C_1 + \frac{4\sqrt{5}}{9} C_2 (13\bar{\rho} - 6) \right] (1-\bar{\rho})^{2/3} + \frac{8B}{\pi} \left[(1-\bar{\rho})^{1/2} - \bar{\rho} \arccos \bar{\rho} \right] \quad (27)$$

$$\Pi_{mo}(\bar{\rho}) = A_1 \left[\omega_1 - \frac{2}{3(1-\bar{\rho})^{1/3}} \right] - B \left(\ln \frac{\bar{\rho}}{2} + 1 \right) \quad (28)$$

with $\gamma_{mo} = 0.696$, $A_1 = 0.3581$, $B = 0.09269$, $\omega_1 = 2.479$, $C_1 = 0.6846$, $C_2 = 0.07098$.

Numerical Results

In this section we compare the MALIKA numerical solution for a fracture propagating in a homogeneous elastic material having a negligible toughness with the corresponding radial solution (25) for a hydraulic fracture propagating in the vis-

cosity dominated regime. For the example considered we used square elements with $\Delta\chi = \Delta\zeta = 1$ and choose $\psi(\tau) = 1$.

In Figure 6 we plot the fracture footprint after 23 time steps, which corresponds to $\tau = 119.28$. The elements in the channel region are colored green, while those in the tip region are colored red. The local fluid velocity vectors are indicated by the scaled red arrows, while the exact fracture front is indicated by the magenta circle. The approximate front positions are indicated by the yellow circles joined by the black line segments. Even for this relatively coarse mesh, the numerical solution is able to locate the circular fluid front relatively accurately. In Figure 7 we plot the cross section of the width surface $\Omega(\chi,\zeta)$ through the plane $\zeta = 0$ for both the numerical solution (solid line) and the exact solution (solid circles) given in (27). There is close agreement between these two solutions. In Figure 8 we plot a similar cross section through the fluid pressure surface $\Pi(\chi,\zeta)$ for both the numerical pressure (solid line) and the exact pressure (solid circles) given (28), which also show remarkable agreement given the coarseness of the mesh. In Figure 9 we compare the numerical fracture radius $\gamma(\tau)$ computed by averaging the interception points between the approximate front segments and the element boundaries over the whole perimeter of the fracture. Initially there are a few ripples in the numerical $\gamma(\tau)$ caused by the fluid in the rows of elements in the north and south of the fracture and the corresponding fluid in the symmetric columns of elements in the east and west of the fracture advancing into the hitherto unfractured rock. If there are very few active elements then these advances have a large impact on the estimate for the fracture radius. However, as time evolves the resolution of the field quantities as well as the fracture front becomes more precise, and these ripples are damped from the solution.

Conclusions

In this paper we have shown that hydraulic fractures propagating in the viscosity dominated regime, which is typical of most stimulation treatments, are characterized by a tip behavior that differs from the classical square root asymptote of linear elastic fracture mechanics. This finding stems from a theoretical analysis of the governing equations and is confirmed by experimental evidence. We have then demonstrated that a hydraulic fracture simulator that embeds the relevant tip asymptote is able to accurately capture a benchmark solution even with a coarse mesh. We should emphasize that the accurate simulation of a fracture propagating in the viscous regime using an algorithm that embeds the LEFM asymptote would require such a dense mesh that it would make the calculations impractical. In fact, we encourage the developers of hydraulic fracture simulators to duplicate the benchmark test that has been documented in this paper.

Acknowledgements

The authors would like to thank Schlumberger for the financial support provided over many years of our efforts to develop a rigorous theoretical framework for the mechanics of fluid-driven fracture. They also recognize the intellectual contribution as well as the commitment to our efforts of Drs. J.

Adachi, J. Desroches, and E. Siebrits of Schlumberger. AB and ED also acknowledge the donors of the American Chemical Society Petroleum Research Fund for partial support of this research.

References

- J.L. Gidley, S.A. Holditch, D.E. Nierode, and R.W. Veatch, editors. *Recent Advances in Hydraulic Fracturing*, volume 12 of *SPE Monograph Series*. Society of Petroleum Engineers, Richardson TX, 1989.
- P. Valkó and M.J. Economides. *Hydraulic Fracture Mechanics*. John Wiley & Sons, Chichester UK, 1995.
- M.J. Economides and C. Boney. Reservoir stimulation in petroleum production. In M.J. Economides and K.G. Nolte, editors, *Reservoir Stimulation*, chapter 1. John Wiley & Sons, Chichester UK, 3rd edition, 2000.
- U. Frank and N. Barkley. Remediation of low permeability subsurface by fracturing enhancements of soil vapor extraction. *Journal of Hazardous Materials*, 40(191–201), 2005.
- L.C. Murdoch. Mechanical analysis of idealized shallow hydraulic fracture. *J. Geotech. Geoenviron.*, 128(6):488–495, 2002.
- L.C. Murdoch and W.W. Slack. Forms of hydraulic fractures in shallow fine-grained formations. *J. Geotech. Geoenviron.*, 128(6):479–487, 2002.
- A.S. Abou-Sayed, D.E. Andrews, and I.M. Buhidma. Evaluation of oily waste injection below the permafrost in Prudhoe Bay field. In *Proceedings of the California Regional Meetings, Bakersfield, CA*, pages 129–142, Richardson, TX, 1989. Society of Petroleum Engineers.
- A.S. Abou-Sayed. Safe injection pressures for disposing of liquid wastes: a case study for deep well injection (SPE/ISRM-28236). In Balkema, editor, *Proceedings of the Second SPE/ISRM Rock Mechanics in Petroleum Engineering*, pages 769–776, 1994.
- C. Young. Controlled-foam injection for hard rock excavation. In *Rock Mechanics for Industry, Proceedings of 37th U.S. Rock Mechanics Symposium, Vail, Colorado, Vol 1*, pages pp.115–122, Rotterdam, 1999. Balkema.
- R.G. Jeffrey and K.W. Mills. Hydraulic fracturing applied to inducing longwall coal mine goaf falls. In *Pacific Rocks 2000*, pages 423–430, Rotterdam, 2000. Balkema.
- A. van As and R.G. Jeffrey. Caving induced by hydraulic fracturing at Northparkes mines. In *Pacific Rocks 2000*, pages 353–360, Rotterdam, 2000. Balkema.
- D.A. Spence and D.L. Turcotte. Magma-driven propagation crack. *J. Geophys. Res.*, 90:575–580, 1985.
- J.R. Lister and R.C. Kerr. Fluid-mechanical models of crack propagation and their application to magma transport in dykes. *J. Geophys. Res.*, pages 10,049–10,077, 1991.
- A.M. Rubin. Propagation of magma-filled cracks. *Ann. Rev. Earth & Planetary Sci.*, 23:287–336, 1995.
- D.D. Pollard and G. Hozlhausen. On the mechanical interaction between a fluid-filled fracture and the earth's surface. *Tectonophysics*, 53:27–57, 1979.
- Y. Fialko. On origin of near-axis volcanism and faulting at fast spreading mid-ocean ridges. *Earth & Plan. Sci. Lett.*, 190:31–39, 2001.
- A.P. Bungler. *Near-Surface Hydraulic Fracture*. PhD thesis, University of Minnesota, 2005.
- S.A. Khristianovic and Y.P. Zheltov. Formation of vertical fractures by means of highly viscous fluids. In *Proc. 4th World Petroleum Congress, Rome*, volume II, pages 579–586, 1955.
- G.I. Barenblatt. On the formation of horizontal cracks in hydraulic fracture of an oil-bearing stratum. *Prikl. Mat. Mech.*, 20:475–486, 1956.
- T.K. Perkins and L.R. Kern. Widths of hydraulic fractures. *J. Pet. Tech., Trans. AIME*, 222:937–949, 1961.
- J. Geertsma and F. de Klerk. A rapid method of predicting width and extent of hydraulic induced fractures. *J. Pet. Tech.*, 246:1571–1581, 1969. (SPE 2458).
- R.P. Nordgren. Propagation of vertical hydraulic fractures. *jpt*, 253:306–314, 1972. (SPE 3009).
- H. Abé, T. Mura, and L.M. Keer. Growth rate of a penny-shaped crack in hydraulic fracturing of rocks. *J. Geophys. Res.*, 81:5335–5340, 1976.
- J. Geertsma and R. Haafkens. A comparison of the theories for predicting width and extent of vertical hydraulically induced fractures. *ASME J. Energy Res. Tech.*, 101:8–19, 1979.
- S.H. Advani, J.S. Torok, J.K. Lee, and S. Choudhry. Explicit time-dependent solutions and numerical evaluations for penny-shaped hydraulic fracture models. *J. Geophys. Res.*, 92(B8):8049–8055, 1987.
- R.J. Clifton and A.S. Abou-Sayed. On the computation of the three-dimensional geometry of hydraulic fractures. In *Proc. SPE Symp. on Low Permeability Gas Reservoirs, Denver*, pages 307–313, Richardson TX, 1979. Society of Petroleum Engineers. (SPE 7943).
- R.J. Clifton and A.S. Abou-Sayed. A variational approach to the prediction of the three-dimensional geometry of hydraulic fractures. In *Proc. SPE/DOE Low Permeability Reservoir Symposium, Denver*. Richardson TX: Society of Petroleum Engineers, 1981. (SPE 9879).
- R.J. Clifton. Three-dimensional fracture-propagation models. In J.L. Gidley, S.A. Holditch, D.E. Nierode, and R.W. Veatch, editors, *Recent Advances in Hydraulic Fracturing – SPE Monographs Vol. 12*, pages 95–108. Society of Petroleum Engineers, 1989.
- S.H. Advani, T.S. Lee, and J.K. Lee. Three dimensional modeling of hydraulic fractures in layered media: Finite element formulations. *ASME J. Energy Res. Tech.*, 112:1–18, 1990. pdf.
- J.L.S. Sousa, B.J. Carter, and A.R. Ingraffea. Numerical simulation of 3D hydraulic fracture using Newtonian and power-law fluids. *Int. J. Rock Mech. Min. Sci. & Geomech. Abstr.*, 30(7):1265–1271, 1993.
- K.R. Shah, B.J. Carter, and A.R. Ingraffea. Hydraulic fracturing simulation in parallel computing environments. *Int. J. Rock Mech. Min. Sci. & Geomech. Abstr.*, 34(3/4):474, 1997.
- A.P. Peirce and E. Siebrits. The scaled flexibility matrix method for the efficient solution of boundary value problems in 2D and 3D layered elastic media. *Computer Meth. Appl. Mech. Eng.*, 190:5935–5956, 2001.
- E. Siebrits and A.P. Peirce. An efficient multi-layer planar 3D fracture growth algorithm using a fixed mesh approach. *Int. J. Numer. Meth. Engng.*, 53:691–717, 2002.
- J.R. Rice. Mathematical analysis in the mechanics of fracture. In H. Liebowitz, editor, *Fracture, an Advanced Treatise*, volume II, chapter 3, pages 191–311. Academic Press, New York NY, 1968.
- D.A. Spence and P.W. Sharp. Self-similar solution for elasto-hydrodynamic cavity flow. *Proc. Roy. Soc. London, Ser. A*, 400:289–313, 1985.
- J.R. Lister. Buoyancy-driven fluid fracture: The effects of material toughness and of low-viscosity precursors. *J. Fluid Mech.*, 210:263–280, 1990.
- J. Desroches, E. Detournay, B. Lenoach, P. Papanastasiou, J.R.A. Pearson, M. Thiercelin, and A.H.-D. Cheng. The crack tip region in hydraulic fracturing. *Proc. Roy. Soc. London, Ser. A*, 447:39–48, 1994.
- R.S. Carbonell, J. Desroches, and E. Detournay. A comparison between a semi-analytical and a numerical solution of a two-

- dimensional hydraulic fracture. *Int. J. Solids Structures*, 36(31–32):4869–4888, 1999.
39. A.A. Savitski and E. Detournay. Propagation of a fluid-driven penny-shaped fracture in an impermeable rock: Asymptotic solutions. *Int. J. Solids Structures*, 39(26):6311–6337, 2002.
40. J.I. Adachi. *Fluid-Driven Fracture in Permeable Rock*. PhD thesis, University of Minnesota, Minneapolis, 2001.
41. J.I. Adachi and E. Detournay. Self-similar solution of a plane-strain fracture driven by a power-law fluid. *Int. J. Numer. Anal. Methods Geomech.*, 26:579–604, 2002.
42. D.I. Garagash and E. Detournay. Plane-strain propagation of a fluid-driven fracture: Small toughness solution. *ASME J. Appl. Mech.*, 72:916–928, November 2005.
43. A.P. Bungler, E. Detournay, and D.I. Garagash. Toughness-dominated hydraulic fracture with leak-off. *Int. J. Fracture*, 134(2):175–190, 2005.
44. D.I. Garagash. Plane-strain propagation of a fluid-driven fracture during injection and shut-in: Asymptotics of large toughness. *Eng. Fract. Mec.*, 73(4):456–481, March 2006.
45. D.I. Garagash. Propagation of plane-strain hydraulic fracture with a fluid lag: Early-time solution. *Int. J. Solids Structures*, 43:5811–5835, 2006.
46. D.I. Garagash. Transient solution for a plane-strain fracture driven by a power-law fluid. *Int. J. Numer. Anal. Methods Geomech.*, 30(14):1439–1475, 2006.
47. J.I. Adachi and E. Detournay. Plane-strain propagation of a fluid-driven fracture in a permeable medium. *Eng. Fract. Mec.*, 2006. Submitted.
48. M.V. Madyarova and E. Detournay. Fluid-driven penny-shaped fracture in permeable rock. *Int. J. Numer. Anal. Methods Geomech.*, 2006. Submitted.
49. A.P. Bungler and E. Detournay. Early time solution for a penny-shaped hydraulic fracture. *ASCE J. Eng. Mech.*, 2006. in press.
50. D.I. Garagash and E. Detournay. The tip region of a fluid-driven fracture in an elastic medium. *ASME J. Appl. Mech.*, 67:183–192, 2000.
51. E. Detournay, J.I. Adachi, and D.I. Garagash. Asymptotic and intermediate asymptotic behavior near the tip of a fluid-driven fracture propagating in a permeable elastic medium. In A.V. Dyskin, X. Hu, and E. Sahouryeh, editors, *Structural Integrity and Fracture*, pages 9–18, Lisse, The Netherlands, 2002. Swets & Zeitlinger.
52. E. Detournay and D.I. Garagash. The near-tip region of a fluid-driven fracture propagating in a permeable elastic solid. *J. Fluid Mech.*, 494:1–32, 2003.
53. S.L. Mitchell, R. Kuske, and A.P. Peirce. An asymptotic framework for the analysis of hydraulic fractures: the impermeable case. *ASME J. Appl. Mech.*, 2006. In press.
54. S. L. Mitchell, R. Kuske, and A.P. Peirce. An asymptotic framework for finite hydraulic fractures including leak-off. *SIAM J. on Appl. Math.*, 2007. in press.
55. A.P. Peirce. Localized Jacobian ILU preconditioners for hydraulic fractures. *Int. J. Numer. Meth. Engng.*, 65(12):1935–1946, 2006.
56. A. P. Peirce and E. Detournay. An Eulerian moving front algorithm with weak form tip asymptotics for modeling hydraulically driven fracture. *Journal of Computational Physics*, 2007. to be submitted.
57. A. P. Bungler and E. Detournay. The tip region in fluid-driven fracture experiments. *J. Mech. Phys. Solids*, 2007. in preparation.
58. A. P. Bungler. A photometry method for measuring the opening of fluid-filled fractures. *Measurement Science and Technology*, 17:3237–3244, 2006.
59. S.L. Crouch and A.M. Starfield. *Boundary Element Methods in Solid Mechanics*. George Allen and Unwin, London, 1983.

60. E. Detournay. Propagation regimes of fluid-driven fractures in impermeable rocks. *Int. J. Geomechanics*, 4(1):1–11, 2004.

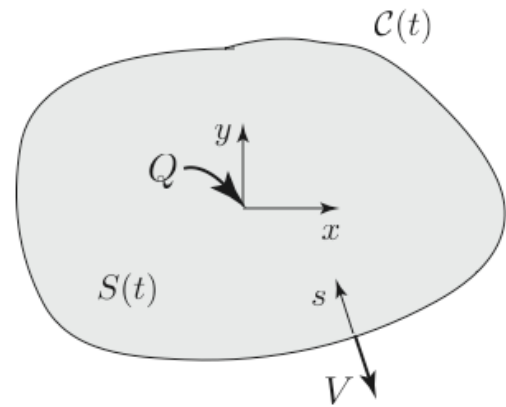


Figure 1: Sketch of a planar fracture.

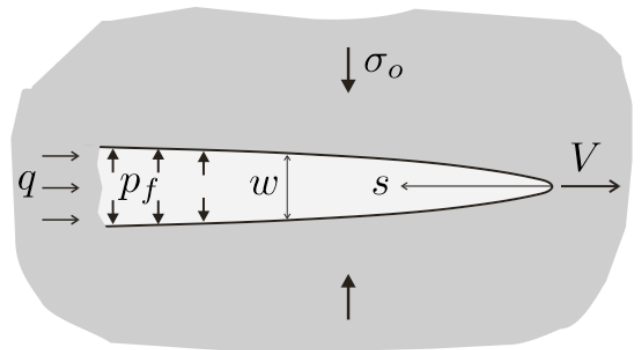


Figure 2: Tip of an advancing fracture.

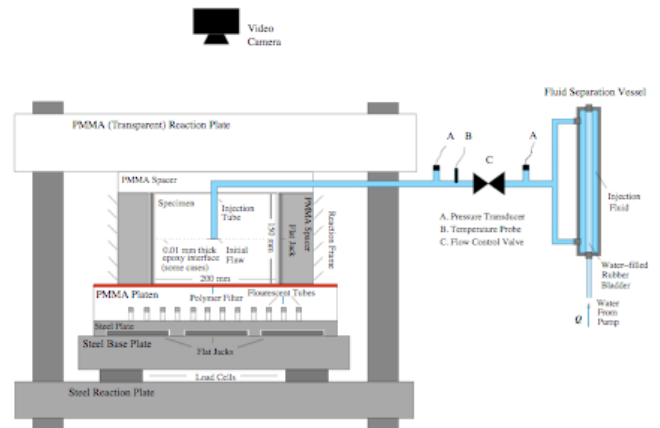


Figure 3: Experimental setup, after [57,58].

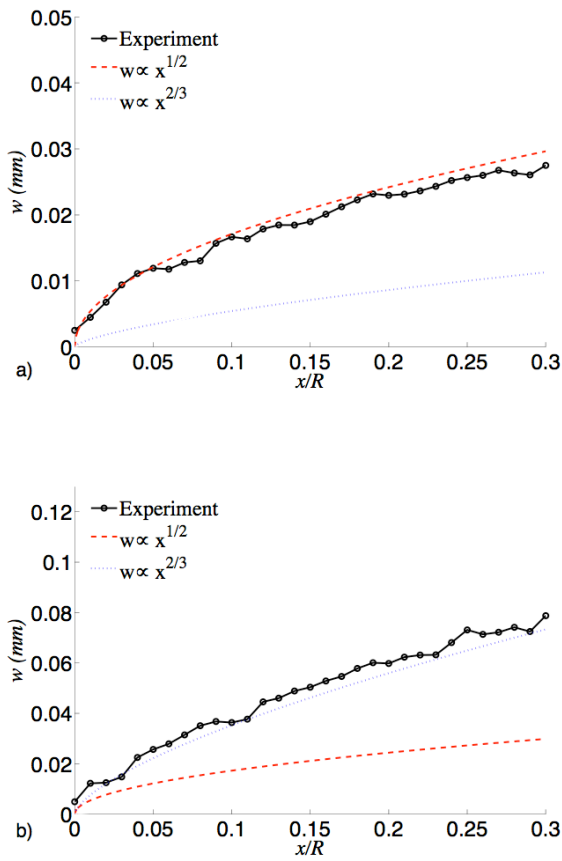


Figure 4: Experimental fracture tip opening along with $w \propto s^{1/2}$ and $w \propto s^{2/3}$ asymptotics for cases where a) the boundary layer thickness \hat{L}_* is much greater than the fracture radius R , and b) the boundary layer thickness \hat{L}_* is approximately the same as R .

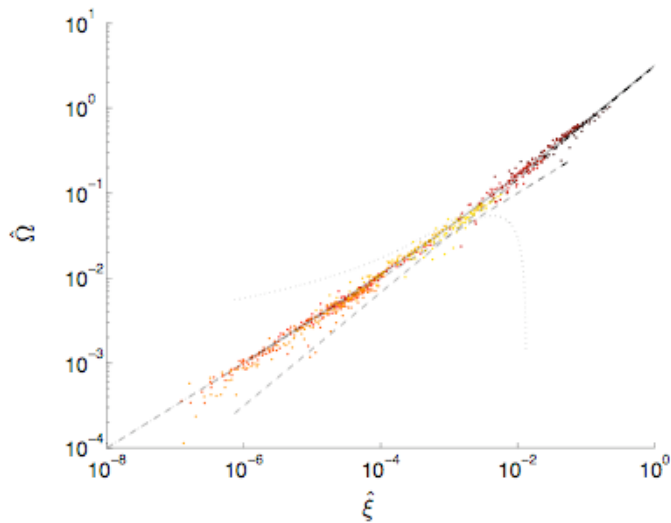


Figure 5: Experimental results, with each experiment indicated by a different color, along with tip solution layer. After [57].

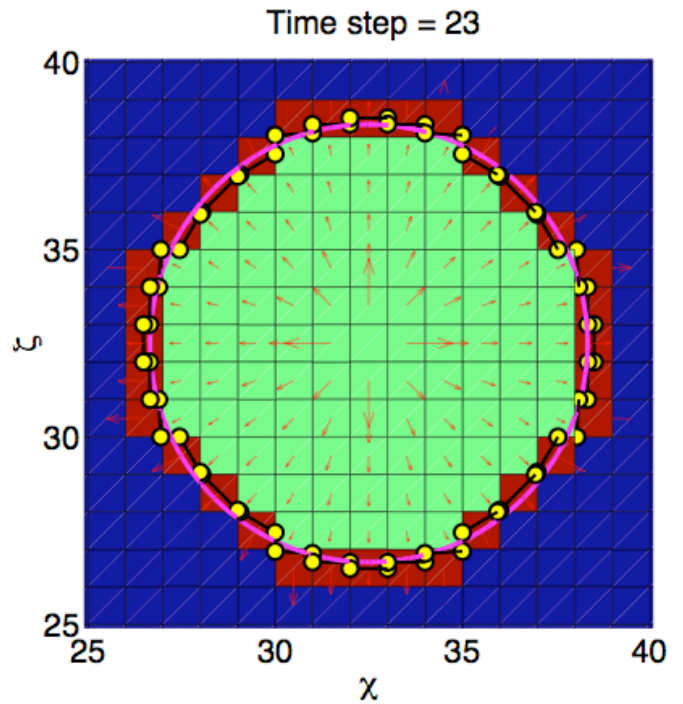


Figure 6: Footprint of fracture after 23 time steps obtained by MALIKA and the exact viscosity dominated solution.

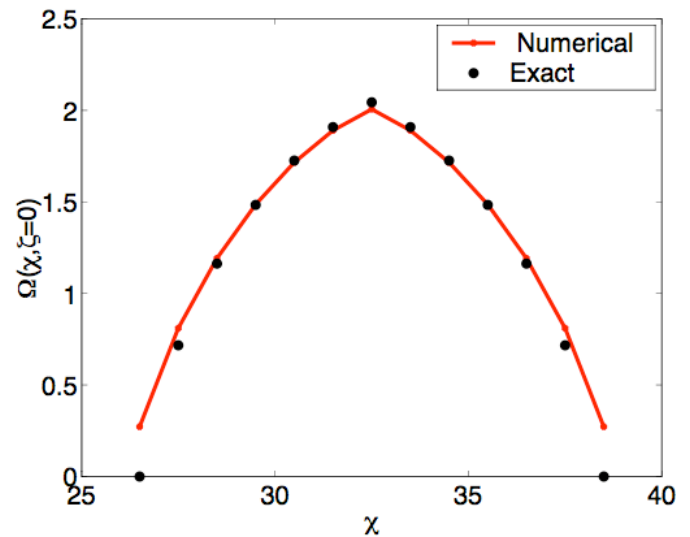


Figure 7: Width profile of the fracture along $\zeta = 0$ after 23 time steps. The MALIKA viscosity dominated solution is compared to the exact solution (25).

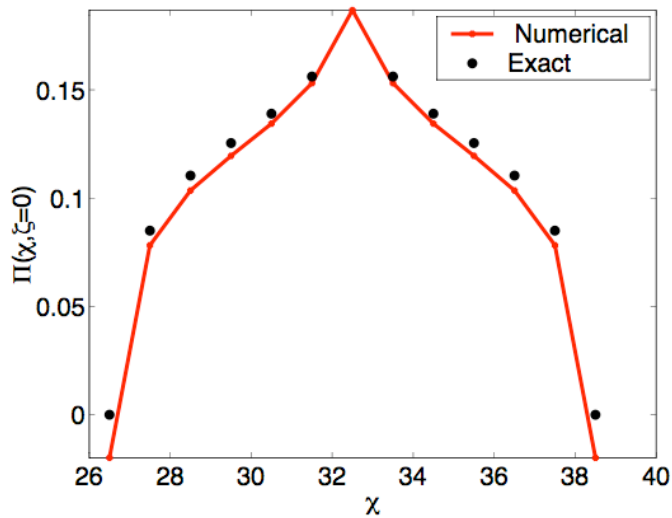


Figure 8: Pressure profile of the fracture along $\zeta = 0$ after 23 time steps. The MALIKA viscosity dominated solution is compared to the exact solution (25).

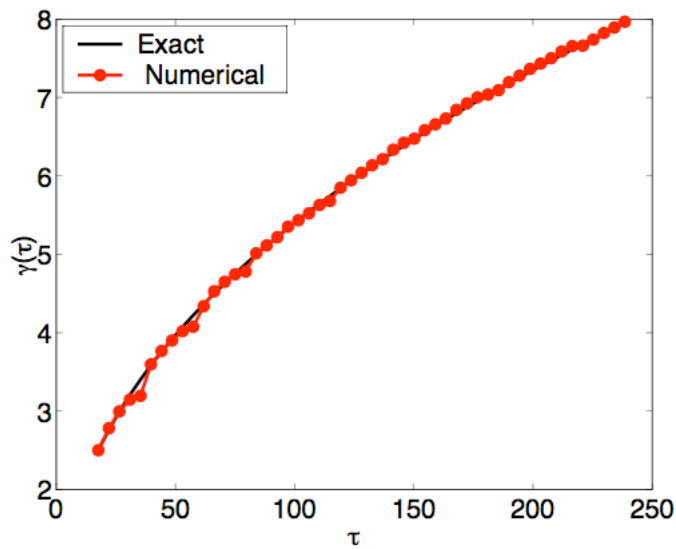


Figure 9: Comparison of fracture radius $\gamma(\tau)$ computed after 50 time steps of calculations with MALIKA and the exact viscosity dominated solution (25).